



1 **Measurement report: Optical properties of carbonaceous aerosols modulated by source**
2 **variations of spring haze**

3 Yuan Cheng¹, Jiu-meng Liu^{1,*}, Xu-bing Cao¹, Yang-mei Guo¹, Ying-jie Zhong¹, Zhi-qing Zhang¹,
4 Ke-bin He²

5 ¹ State Key Laboratory of Urban-rural Water Resource and Environment, School of Environment,
6 Harbin Institute of Technology, Harbin, 150090, China

7 ² State Key Laboratory of Regional Environment and Sustainability, School of Environment,
8 Tsinghua University, Beijing 100084, China

9 Corresponding author. Jiu-meng Liu (jiumengliu@hit.edu.cn).

10 **Abstract**

11 Carbonaceous aerosols exert unique impacts on earth energy balance, but are not well constrained
12 in air quality and climate models yet. In this study, a field campaign was conducted in Northeast
13 China during a spring season to explore the optical properties of carbonaceous aerosols modulated
14 by dramatic variations of particulate matter sources. We first integrated the light absorption results
15 derived from different methods, including both on-line and off-line approaches. Then by
16 synthesizing a series of source-relevant signatures, three types of haze episodes were identified. In
17 general, agricultural fire emissions exerted strong influences on brown carbon (BrC), by effectively
18 increasing the mass absorption efficiency (MAE) of bulk BrC, and emitting chromophores with a
19 characteristic absorption peak at ~365 nm. Specifically, fires with low combustion efficiencies were
20 more capable of enhancing the impacts of BrC on bulk aerosol absorption, and were more favorable
21 for the emissions of organic compounds with relatively high molecular weights and aromatic
22 contents. In addition, the agricultural fires, especially those with relatively low efficiencies, resulted
23 in overestimations of black carbon (BC) mass by thermal-optical method due to unique emitted
24 species. By excluding the impacts from agricultural fires and dusts, we unfolded the influence of



- 25 secondary aerosol formation on the MAE of BC (MAE_{BC}). With the enhancement of secondary
- 26 aerosols, MAE_{BC} was found to exhibit a clear increasing trend, which could be translated into the
- 27 light absorption enhancement (E_{abs}) factors of up to ~ 2.3 .



28 **1. Introduction**

29 Carbonaceous aerosols, which consist of organic compounds and black carbon (BC), exert
30 unique impacts on earth energy balance (Bond et al., 2013), e.g., through absorbing and scattering
31 solar radiation, influencing cloud processes, and deposition on ice and snow cover. However, as a
32 complex mixture of compounds with continuing changes in chemical and physical properties
33 (Pöschl, 2005; Andreae and Gelencsér, 2006), carbonaceous aerosols remained poorly constrained
34 in air quality and climate models. For example, challenges still existed in the simulation of the
35 sources, abundances, optical properties and radiative forcing of BC (Samset et al., 2014; Winiger et
36 al., 2019; Gao et al., 2022; Chen et al., 2025; Wang et al., 2025). Similarly, discrepancies in the
37 modeled and observed results were also evident for organic aerosol (OA), e.g., as indicated by the
38 difficulties in proper predictions of primary OA emitted by open burning (Zhong et al., 2023),
39 secondary OA (SOA) formed by volatility organic compounds (VOCs) with relatively low
40 saturation vapor concentrations (Chang et al., 2022), and light absorbing OA, i.e., brown carbon
41 (Tuccella et al., 2025). On one hand, state-of-the-art models were subject to various uncertainties
42 such as those associated with the emission inventories, the treatments of BC lifetime and mixing
43 state, the formation pathways of SOA, and the parameterization of brown carbon. On the other hand,
44 there were also uncertainties in the observational results of carbonaceous aerosols. For example,
45 measured BC were frequently found to differ by several times among various detection approaches
46 (Tinorua et al., 2025), none of which has been established as a reference method (Petzold et al.,
47 2013). In addition, it was commonly believed that inter-method differences in BC results were
48 closely related to aerosol sources, but the influencing factors at play were not well understood (Pileci
49 et al., 2021). Thus, largely constrained by the multitude of measurement principles, it remained



50 challenging to integrate the observational and the subsequent interpretation (e.g., source
51 apportionment) results on carbonaceous aerosols across studies and regions (Putaud et al., 2025).

52 In China, the ambient fine particulate matter (PM_{2.5}) pollution has been reduced substantially
53 since 2013 (Geng et al., 2024), driven by a series of national-level policies including the *Action Plan*
54 *for Air Pollution Prevention and Control* (2013–2017), the *Three-Year Action Plan for Winning the*
55 *Blue Sky Defense Battle* (2018–2020) and the *Action Plan for Continuous Improvement of Air*
56 *Quality* (2023–2025). More recently, a new round of revisions for the Ambient Air Quality
57 Standards were launched by the Ministry of Ecology and Environment (MEE) of China, e.g., the
58 Class 2 standards of PM_{2.5} will be tightened from 35 to 25 µg/m³ for annual average and from 75 to
59 50 µg/m³ for 24-hour average (National Public Service Platform for Standards Information, 2025).
60 The revised standards, which are expected to be officially released soon, provide new impetus for
61 air quality improvement and meanwhile place great demands on a stronger observational support
62 for PM_{2.5} pollution control. This is particularly the case for Northeast China, which was overlooked
63 by all of the three action plans implemented during 2013–2025 and showed relatively slow
64 decreasing rate of PM_{2.5} (Xiao et al., 2022).

65 Northeast China comprises three provinces (i.e., Liaoning, Jilin and Heilongjiang) and involves
66 two national-level city clusters, i.e., Harbin-Changchun (HC) and Central-Southern Liaoning.
67 Among the two city-cluster regions, HC differs more significantly from the traditional hotspots for
68 air pollution control, e.g., Beijing and the surrounding areas. The distinctiveness of HC could be
69 seen from two aspects (Cheng and He, 2026). First, HC is located in a severe cold climate region
70 (e.g., with a seasonal average of –15 °C in Harbin), leading to intensive energy use in the cold
71 winters for heating and thus high emissions of anthropogenic pollutants. Second, HC is within a



72 major agricultural region, where open burning of crop residues remains prevalent after autumn
73 harvesting and before spring planting in the next year. The agricultural fires frequently resulted in
74 heavy pollution episodes, e.g., with record-high PM_{2.5} concentration of ~2350 µg/m³ (1-hour
75 average) in Harbin (Cheng et al., 2021). Despite the distinct emission sources, the aerosols in HC
76 (e.g., regarding their chemical compositions, source contributions, optical properties and impacts)
77 have not been comprehensively explored, as indicated by the limited number of studies available
78 (e.g., Wu et al., 2020; Zhang et al., 2020; Xie et al., 2024).

79 By combining on-line and off-line measurements, a field campaign was conducted in the
80 central city of HC during a period with dramatic variations of aerosol sources and compositions.
81 From a technical perspective, we elucidated the inter-method discrepancies in light absorption
82 coefficients of carbonaceous aerosols, including both black and brown carbon. From a scientific
83 perspective, we highlighted the signatures of various types of episodes and unfolded the responses
84 of aerosol optical properties to agricultural fire emissions and second aerosol formation. We also
85 demonstrated that nocturnal nitrate formation could be effectively enhanced by agricultural fires,
86 and thermal-optical measurement of BC mass could be subject to substantial artifacts during specific
87 episodes. This study provided insights into the links between optical and chemical properties of
88 aerosols in Northeast China, which are essential for understanding the haze pollution in this distinct
89 but largely unexplored region.

90 **2. Methods**

91 **2.1 On-line observations**

92 Aerosol optical properties and mass concentrations of gaseous pollutants were measured with
93 high time resolutions for about one month (from April 1 to May 2, 2023) in Harbin. The observation



94 was performed on the campus of Harbin Institute of Technology (HIT), an urban site surrounded by
95 residential and commercial areas. For aerosol measurements, ambient air was drawn into a stainless-
96 steel sampling line at a flow rate of 16.7 L/min, using a vacuum pump (VACUUBRAND, Wertheim,
97 Germany) and a mass flow controller (Alicat Scientific Inc., AZ, USA). After passing through a
98 PM_{2.5} cyclone (URG-2000-30EH; URG Corp., NC, USA) and a Nafion dryer (MD-700; Perma Pure
99 LLC, NJ, USA), the sampled aerosols were measured by a photoacoustic extinctionsmeter (PAX;
100 Droplet Measurement Technologies LLC, CO, USA) and a dual-spot Aethalometer (AE33; Aerosol
101 d.o.o., Ljubljana, Slovenia). The PAX was operated at a wavelength (λ) of 870 nm based on *in-situ*
102 measurement approaches, i.e., photoacoustic method for the light absorption coefficient (b_{abs}) and a
103 wide-angle integrating reciprocal nephelometer for the scattering coefficient (b_{scat}). The single
104 scattering albedo (SSA) was calculated as the ratio of b_{scat} to extinction coefficient (b_{ext} , the sum of
105 b_{abs} and b_{scat}). In addition, the AE33, which was operated with M8060 filter tapes, provided aerosol
106 absorption coefficients at seven wavelengths (i.e., 370, 470, 520, 590, 660, 880 and 950 nm). It has
107 been widely acknowledged that filter-based absorption measurement could be biased by the loading
108 effect and the multiple scattering effect (Weingartner et al., 2003; Collaud Coen et al., 2010). For
109 AE33, the former had been accounted for by a compensation algorithm based on absorption
110 measurements from two differently loaded filter spots (Drinovec et al., 2015), while the latter was
111 typically corrected using an empirical parameter (C). The manufacture recommended a constant of
112 1.39 for C , but the experimentally determined C values were frequently found to deviate
113 considerably from the suggested value, with tempo-spatial variations and dependences on aerosol
114 properties (Ferrero et al., 2021; Yus-Díez et al., 2021, 2025; Renzi et al., 2026). In this study, the
115 default multiple scattering correction (assuming $C = 1.39$) was not applied and the corresponding



116 absorption coefficients, which had only been corrected for the loading effect, will be specified as
117 $(b_{\text{abs}})^*$. Refer to Supplement for a more detailed description of $(b_{\text{abs}})^*$. The aerosol absorption
118 Ångström exponent (AAE_{bulk}) was determined as the slope derived from the linear regression of
119 $\ln[(b_{\text{abs}})^*]$ against $\ln(\lambda)$, in the wavelength range of 370–880 nm.

120 For the measurement of gaseous pollutants, ambient air was filtered and then drawn into a
121 PTFE sampling line. A non-dispersive infrared analyzer (XHCO2000B) was used to measure carbon
122 monoxide (CO), and two chemiluminescence-based analyzers (XHOZ7000 and XHN2000B) were
123 operated to determine ozone (O_3) and nitrogen dioxide (NO_2), respectively. The instruments were
124 manufactured by Hebei Sailhero Inc. (Shijiazhuang, China) in compliance with the reference
125 methods released by the Ministry of Ecology and Environment of China.

126 The time resolutions were 1 second for PAX and 1 minute for the other instruments. Thus the
127 raw results from PAX were converted to 1-minute averages before further analyses. The on-line
128 measurement results were summarized in Figure 1.

129 **2.2 Off-line measurements**

130 Daytime and nighttime $\text{PM}_{2.5}$ samples were collected at the same site with the on-line
131 instruments during the campaign. The sampling was done by a mass flow controlled high-volume
132 sampler (TE-6070BLX-2.5-HVS; Tisch Environmental Inc., OH, USA), which was operated at a
133 flow rate of $1.13 \text{ m}^3/\text{min}$ using pre-baked quartz-fiber filters (Pall Corp., NY, USA). To avoid rush
134 hours, the daytime and nighttime samples were collected from 9:00 to 16:00 and from 21:00 to 5:00
135 of the next day, respectively.

136 Organic carbon (OC) and elemental carbon (EC) of the filter samples were measured by a
137 thermal/optical carbon analyzer (DRI-2001; Atmoslytic Inc., CA, USA), using the IMPROVE-A

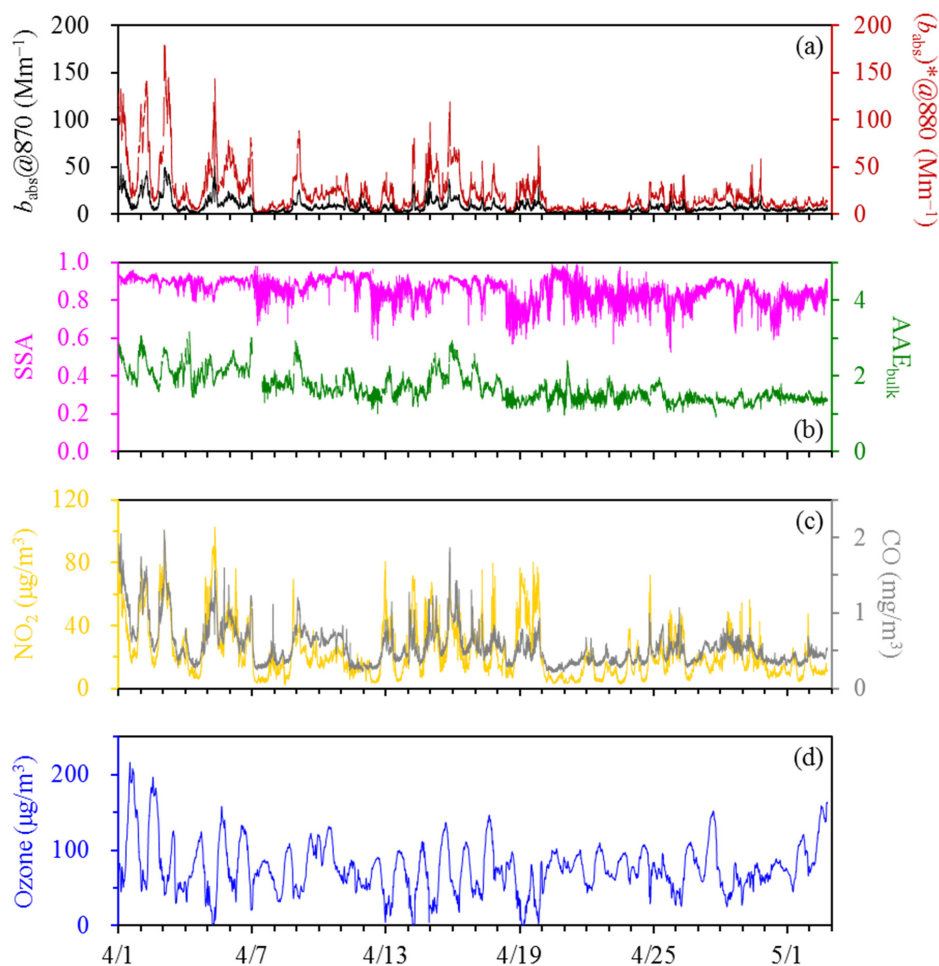


138 temperature protocol with the transmittance charring correction. The carbon analyzer also provided
139 optical attenuation (ATN) results for the filter samples. ATN was calculated as $\ln(I_{\text{final}}/I_{\text{initial}})$, where
140 I_{initial} and I_{final} indicate the filter transmittance signals (I) measured at the beginning (i.e., when the
141 particle-laden filter has not been heated) and the end (i.e., when all the deposited carbon has been
142 combusted off the filter) of thermal-optical analysis, respectively. Then the absorption coefficient
143 (Mm^{-1}) could be determined as $\text{ATN} \times A/V$, where A is the filter area loaded with particles (mm^2)
144 and V is the volume of the air sampled (m^3). It should be noted that when using the carbon analyzer,
145 the absorption coefficients were derived at a single wavelength of 632 nm without any correction,
146 for either the loading effect or the multiple scattering effect.

147 Water extracts of the filter samples were analyzed for inorganic ions using an ion
148 chromatography system. The samples were also extracted by methanol to measure brown carbon
149 (BrC). Light absorption spectra of the methanol extracts were detected over the wavelength range
150 of 200–1110 nm, using a spectrophotometer (Ocean Optics Inc., FL, USA) coupled with a 2.5m
151 long liquid waveguide capillary cell (LWCC; World Precision Instruments Inc., FL, USA). The
152 absorption coefficients determined in this approach, which were actually the absorption coefficients
153 of the dissolved brown carbon (i.e., methanol-soluble BrC), will be referred to as $(b_{\text{abs}})_{\text{MS-BrC}}$.

154 **2.3 Open-access data**

155 Air quality data, e.g., hourly $\text{PM}_{2.5}$ and PM_{10} concentrations, were obtained from a nearby air
156 quality monitoring site (~2 km away from the HIT site) operated by the China National
157 Environmental Monitoring Center (CNEMC; <https://air.cnemc.cn:18007/>). Meteorological data
158 (e.g., temperature, relative humidity and wind speed) were obtained with a time resolution of 1
159 hour from Weather Underground (<https://www.wunderground.com/>).



160

161 **Figure 1.** Time series of (a) the PAX-based b_{abs} at 870 nm and the AE33-based $(b_{\text{abs}})^*$ at 880 nm,
 162 (b) the PAX-based SSA and the AE33-based AAE_{bulk} , (c) NO_2 and CO, and (d) ozone. The results
 163 were shown with a time resolution of 1 minute.

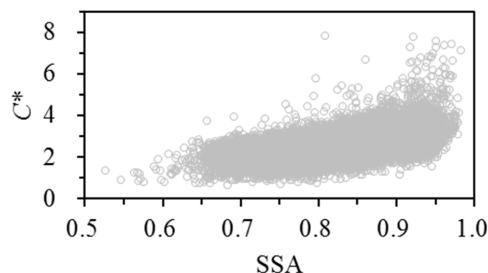
164 **3. Results and discussion**

165 **3.1 Integrating optical parameters derived from different methods**

166 We first compared the light absorption coefficients derived from the PAX at 870 nm and from
 167 the AE33 at 880 nm, which will be termed $b_{\text{abs}@870}$ and $(b_{\text{abs}})^*@880$, respectively. The $b_{\text{abs}@870}$
 168 results were not subject to artifacts associated with filter-based absorption measurement, as they



169 were obtaining using *in-situ* technology. For $(b_{\text{abs}})^*_{@880}$, although the loading effect had been
170 accounted for, other artifacts still existed, which could be attributed mainly to the multiple scattering
171 by the filter fibers and the scattering by the particles embedded in the filter. The experimental setup
172 used in this study did not allow distinguishing the two artifacts. However, their overall effect could
173 be determined by comparing $(b_{\text{abs}})^*_{@880}$ with $b_{\text{abs}}_{@870}$. The $(b_{\text{abs}})^*_{@880}$ to $b_{\text{abs}}_{@870}$ ratios, which
174 will be termed C^* , generally exhibited a normal distribution for the spring campaign, with a mean
175 of 2.67 and a standard deviation of 0.54 (Figure S1). The values suggested that the overall effect of
176 multiple scattering and aerosol scattering resulted in a significant overestimation of light absorption
177 by $(b_{\text{abs}})^*_{@880}$. Further investigations indicated that the variation of C^* was closely related to SSA
178 (Figures 2 and S2; Table 1). The median C^* was as low as 1.24 for the lower end of SSA (below
179 0.60) encountered in the spring campaign. Then C^* increased sharply as SSA became higher, e.g.,
180 with a median of 2.06 for the SSA range of 0.65–0.70. However, the variation of C^* was largely
181 flattened when SSA further increased. For example, compared to that observed for the SSA range
182 of 0.65–0.70, the median C^* was only ~0.4 higher when SSA reaching 0.80–0.85. Finally, with
183 increasing SSA, the increase of C^* became sharp again, e.g., with a median C^* of 3.27 for the higher
184 end of SSA (0.95–1.00). The clear dependence of C^* on SSA suggested the limitation of using a
185 fixed value for the scattering-associated correction in filter-based absorption measurement. To
186 enhance the relevance of time-resolved C^* to future studies, the median values of C^* were presented
187 in Table 1 for various SSA bins (from below 0.60 to above 0.95), which covered the typical SSA
188 levels observed for ambient conditions. We applied the SSA-dependent median C^* (Table 1) to AE33
189 and found that the corrected $(b_{\text{abs}})^*_{@880}$ were in reasonable agreement with $b_{\text{abs}}_{@870}$ (Figure 3a),
190 demonstrating the practicability of the SSA-dependent C^* results.



191

192 **Figure 2.** Dependence of C^* on SSA, both of which had a time resolution of 1 minute. Results
 193 involved in this figure were for the entire measurement period.

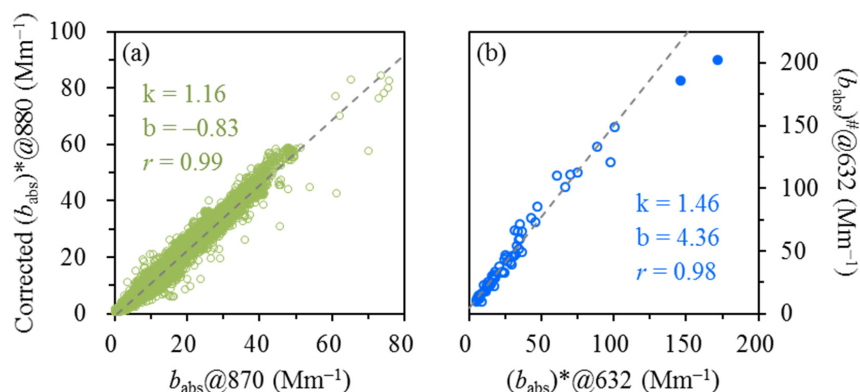
194 **Table 1.** SSA-dependent C^* results determined during the spring campaign.

SSA range	0.50– 0.60	0.60– 0.65	0.65– 0.70	0.70– 0.75	0.75– 0.80	0.80– 0.85	0.85– 0.90	0.90– 0.95	0.95– 1.00
Median C^*	1.24	1.65	2.06	2.24	2.26	2.46	2.76	3.06	3.27
Lower quartile of C^*	0.90	1.34	1.66	1.78	1.89	2.17	2.46	2.72	2.91
Upper quartile of C^*	1.35	2.07	2.40	2.53	2.62	2.77	3.07	3.40	3.92

195 We then compared the light absorption coefficients determined by the AE33 and off-line carbon
 196 analyzer. The off-line results, which were obtained at 632 nm with no correction, will be specified
 197 as $(b_{\text{abs}})^{\#}@632$. To align with $(b_{\text{abs}})^{\#}@632$, the AE33-based absorption coefficients at the same
 198 wavelength, i.e., $(b_{\text{abs}})^{*}@632$, were converted from the directly-measured $(b_{\text{abs}})^{*}$ at 660 nm using
 199 AAE_{bulk} , which described the wavelength dependence of $(b_{\text{abs}})^{*}$. As shown in Figure 3b, the off-line
 200 measurements always resulted in higher absorption coefficients compared to AE33, and their
 201 relationship could be approximated by the following linear function: $(b_{\text{abs}})^{\#}@632 = 1.46 \times$
 202 $(b_{\text{abs}})^{*}@632 + 4.36$ ($r = 0.98$). A likely cause for the observed discrepancies was the difference in
 203 filter media used by the two instruments. As stated in the Methods section, the carbon analyzer used
 204 quartz filters, whereas the AE33 was operated with M8060 filter tapes. Although the material of
 205 M8060 was not specified by the AE33 manufacture, the multiple scattering correction factors of



206 M8060 were determined to be generally comparable with the previously used M8020 (i.e., PTFE-
207 coated glass-fiber filter), e.g., with relative standard deviations of within 5% for different types of
208 sites in Europe (Yus-Díez et al., 2021). Field campaigns conducted at various locations suggested
209 that compared to M8020, quartz filter showed stronger multiple scattering effect and thus required
210 a higher correction factor, e.g., 2.14 vs. 1.57 for the fresh aerosols in Klagenfurt, Austria (Drinovec
211 et al. (2015) and 3.43 vs. 2.64 for the aged aerosols in Milan, Italy (Ferrero et al., 2021). This
212 indicated that when running two AE33 side-by-side with different filter media, quartz filter would
213 lead to higher $(b_{\text{abs}})^{\#}$ than M8020, by factors of about 1.3–1.4. A comparable discrepancy was
214 observed in St. Louis for the absorption coefficients measured by quartz and glass-fiber filters,
215 which differed by a factor of 1.41 (Snyder and Schauer, 2007). These ratios (~ 1.3 – 1.4) were close
216 to the slope shown in Figure 3b, indicating that the $(b_{\text{abs}})^{\#}@632$ vs. $(b_{\text{abs}})^{*}@632$ discrepancies could
217 be attributed primarily to the use of different filters in off-line and on-line measurements. In addition,
218 it was noticed that the linear dependence of $(b_{\text{abs}})^{\#}@632$ on $(b_{\text{abs}})^{*}@632$ did not hold for the two
219 heavily-loaded samples collected on the nights of April 1 and 2, 2023, which showed the highest
220 carbon loadings (above $115 \mu\text{g}/\text{cm}^2$ for the sum of OC and EC) and $\text{PM}_{2.5}$ concentrations
221 (exceeding $165 \mu\text{g}/\text{m}^3$) throughout the campaign. For these two samples, the ratios of $(b_{\text{abs}})^{\#}@632$
222 to $(b_{\text{abs}})^{*}@632$ were only 1.27 and 1.18, respectively. It appeared that the absorption coefficients
223 derived from the carbon analyzer could be biased low at high filter loadings. This artifact was to
224 some extent similar to the loading effect in the Aethalometer measurement but seemed unapparent
225 at relatively low filter loadings.



226

227 **Figure 3. (a)** Comparison of the corrected $(b_{\text{abs}})^*_{@880}$ and the PAX-based $b_{\text{abs}}@870$ for the entire
 228 measurement period. The two parameters had the same time resolution of 1 minute and showed a
 229 median RSD (relative standard deviation) of 8.5%. The correction of $(b_{\text{abs}})^*_{@880}$ was based on the
 230 median C^* values in Table 1. **(b)** Comparison of $(b_{\text{abs}})^{\#}_{@632}$ and $(b_{\text{abs}})^*_{@632}$. The former was
 231 directly derived from the carbon analyzer without any correction, while the latter was obtained by
 232 extrapolating the AE33-based $(b_{\text{abs}})^*_{@660}$ to 632 nm. The time-resolved $(b_{\text{abs}})^*_{@632}$ results were
 233 first averaged for the filter sampling segments and then compared to the off-line $(b_{\text{abs}})^{\#}_{@632}$. In (a)
 234 and (b), the dashed lines indicate the linear regression results with k as the slope and b as the
 235 intercept. In (b), the linear dependence did not hold for two heavily loaded filters which were
 236 highlighted by the solid circles.

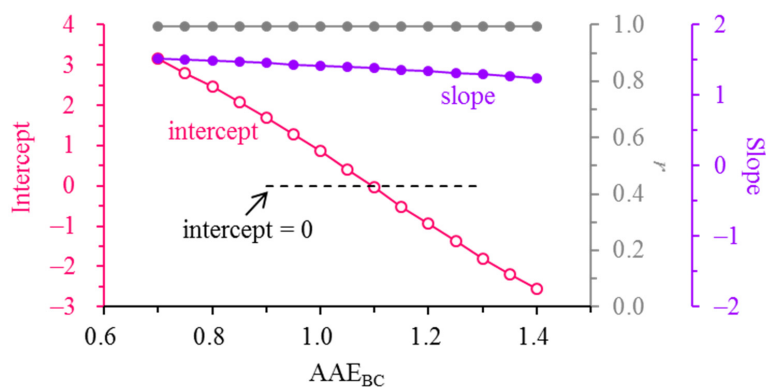
237 We also compared the brown carbon results measured by the AE33 and off-line (i.e., methanol
 238 extraction) approaches. It has been widely accepted that methanol could dissolve the vast majority
 239 (e.g., ~90%) of organic aerosol, making methanol-soluble OC (MSOC) a frequently-used surrogate
 240 for BrC (Laskin et al., 2015, 2025). The absorption coefficients of MSOC, which were directly
 241 measured, will be primarily investigated at 365 nm and the corresponding results will be termed
 242 $(b_{\text{abs}})_{\text{MS-BrC}}@365$. For AE33, the absorption coefficient of BrC at 370 nm was calculated as:

$$243 \quad (b_{\text{abs}})_{\text{BrC}}@370 = b_{\text{abs}}@370 - b_{\text{abs}}@880 \times (880/370)^{\text{AAE}_{\text{BC}}} \quad (1)$$

244 In Equation (1), $(b_{\text{abs}})@370$ and $(b_{\text{abs}})@880$ indicate the absorption coefficients at 370 and 880 nm,
 245 respectively, both of which had been corrected for the scattering-associated artifacts using the C^*
 246 values in Table 1; AAE_{BC} is the absorption Ångström exponent of black carbon, a parameter



247 describing the wavelength dependence of BC-induced light absorption. Two assumptions were
248 involved in the calculation, including (i) the light absorption coefficient measured at 880 nm could
249 be attributed only to black carbon and (ii) the coefficients observed at shorter wavelengths could be
250 broken down into the contributions from BC and BrC (Lack and Langridge, 2013). A variety of
251 AAE_{BC} were tested in this study, first from 0.7 to 1.4 with an increment of 0.05. As shown in Figure
252 4, the AE33-based $(b_{abs})_{BrC@370}$ and the solution-based $(b_{abs})_{MS-BrC@365}$ kept strong correlation
253 (with r staying above 0.99) regardless of the values assumed for AAE_{BC} . In addition, when
254 increasing the AAE_{BC} from 0.7 to 1.4, the regression slope decreased slowly from 1.52 to 1.24
255 whereas the intercept changed sharply from +3.16 to -2.56. The intercept turned from a positive
256 value into negative when the AAE_{BC} was changed from 1.05 to 1.10. Thus we further tested various
257 AAE_{BC} values in this range with a smaller increment of 0.01. The intercept was found to be closest
258 to zero (-4.1×10^{-2}) for an AAE_{BC} value of 1.10 (Figure S3), e.g., compared to an intercept of
259 $+5.2 \times 10^{-2}$ for an AAE_{BC} of 1.09. It appeared that a reasonable correlation could be reached for the
260 on-line and off-line BrC results by assuming $AAE_{BC} = 1.10$. However, a slope of 1.38 retrieved
261 under this assumption suggested that the AE33-based absorption coefficients of BrC were
262 considerably higher than results from the methanol extracts of filter samples. This discrepancy
263 should be associated with the states of the measured BrC, since particulate brown carbon has been
264 found to show higher absorption coefficients than dissolved BrC (Liu et al., 2013; Washenfelder, et
265 al., 2015). Another likely cause for this discrepancy was the OC insoluble in methanol (MIOC),
266 which could be a considerable contributor to BrC absorption but was missed by the solution-based
267 approach for BrC determination (Atwi et al., 2022).



268

269 **Figure 4.** Slope, intercept and r determined by regressing the AE33-based $(b_{\text{abs}})_{\text{BrC}@370}$ against the
 270 solution-based $(b_{\text{abs}})_{\text{MS-BrC}@365}$. Different AAE_{BC} values were assumed to retrieve the time-
 271 resolved $(b_{\text{abs}})_{\text{BrC}@370}$, which were first averaged for the filter sampling segments and then used
 272 for the regression.

273 3.2 Identification of different episodes

274 There have been numerous evidences suggesting pronounced influences of aerosol sources on
 275 the mass absorption efficiency of brown carbon (MAE_{BrC}), which is defined as the ratio of BrC's
 276 absorption coefficient to its mass concentration. For example, regarding seasonal variations,
 277 MAE_{BrC} typically peaked in winter due to increased emissions from coal combustion and/or biomass
 278 burning (Mo et al., 2024). In addition, MAE_{BrC} were found to show diurnal variations with higher
 279 nighttime levels during winter in Northeast China, and this pattern was inferred to be driven
 280 primarily by the emissions from heavy-duty diesel trucks, which were allowed to operate only at
 281 night for the main urban area (Cheng et al., 2023). Spatial variations were also evident for MAE_{BrC} ,
 282 e.g., water-soluble BrC, which was strongly associated with SOA, was observed to be more
 283 absorbing in Los Angeles compared to Atlanta (Zhang et al., 2011). In that study, SOA were traced
 284 back mainly to anthropogenic VOCs for Los Angeles, and to biogenic precursors for Atlanta. The
 285 authors then speculated that secondary BrC from anthropogenic precursors likely had stronger



286 capacities of light absorption compared to biogenic SOA, while this inference was confirmed shortly
287 by chamber studies (Lambe et al., 2013; Liu et al., 2016).

288 Given its close association with aerosol sources, in this study, MAE_{BrC} was first investigated
289 to distinguish different types of pollution episodes. To avoid the omission of MIOC contribution,
290 we applied the bulk BrC light absorption from AE33 and calculated MAE_{BrC} as the ratio of
291 $(b_{abs})_{BrC@370}$ to OC. For each filter sample, the off-line OC was used as BrC mass while the
292 corresponding BrC absorption coefficient took the average of the AE33-based results during the
293 filter sampling period. The MAE_{BrC} results were found to vary significantly (from 0.12 to 3.23
294 m^2/gC) during the spring campaign, pointing to changeable drivers for the haze pollution. Two
295 groups of samples were most noticeable, showing MAE_{BrC} levels at the lower and higher ends of
296 the spring results, respectively. The first group ($N = 13$, case A in Figure 5) had a MAE_{BrC} range of
297 0.12 to 0.40 m^2/gC (Figure 5a), and the samples exhibited the following characteristics (Figures 5b–
298 5d): relatively low ratios of $PM_{2.5}$ to PM_{10} (0.15 in terms of median value; same hereafter), relatively
299 high wind speeds (8.77 m/s), and relatively low ratios of K^+ to sulfate (0.18). The $PM_{2.5}$ to PM_{10}
300 ratio ($PM_{2.5}/PM_{10}$) was strongly related to the dust influence, typically with a decreasing trend as
301 the dust impact became stronger (Putaud et al., 2010). Thus for the first group of samples, the
302 reduced $PM_{2.5}/PM_{10}$ together with the elevated wind speeds presumably indicated considerable
303 influences of dusts. In addition, observational results from Northeast China suggested that
304 agricultural fires could effectively enhance the abundances of K^+ but was not a significant
305 contributor to sulfate (Cheng et al., 2021), resulting in spikes of K^+ to sulfate ratios ($K^+/sulfate$) that
306 typically coincided with the peaks of levoglucosan to OC ratios (LG/OC). Thus similar to increased
307 LG/OC, enhanced $K^+/sulfate$ could also be used as an indicator for agricultural fires. Conversely,

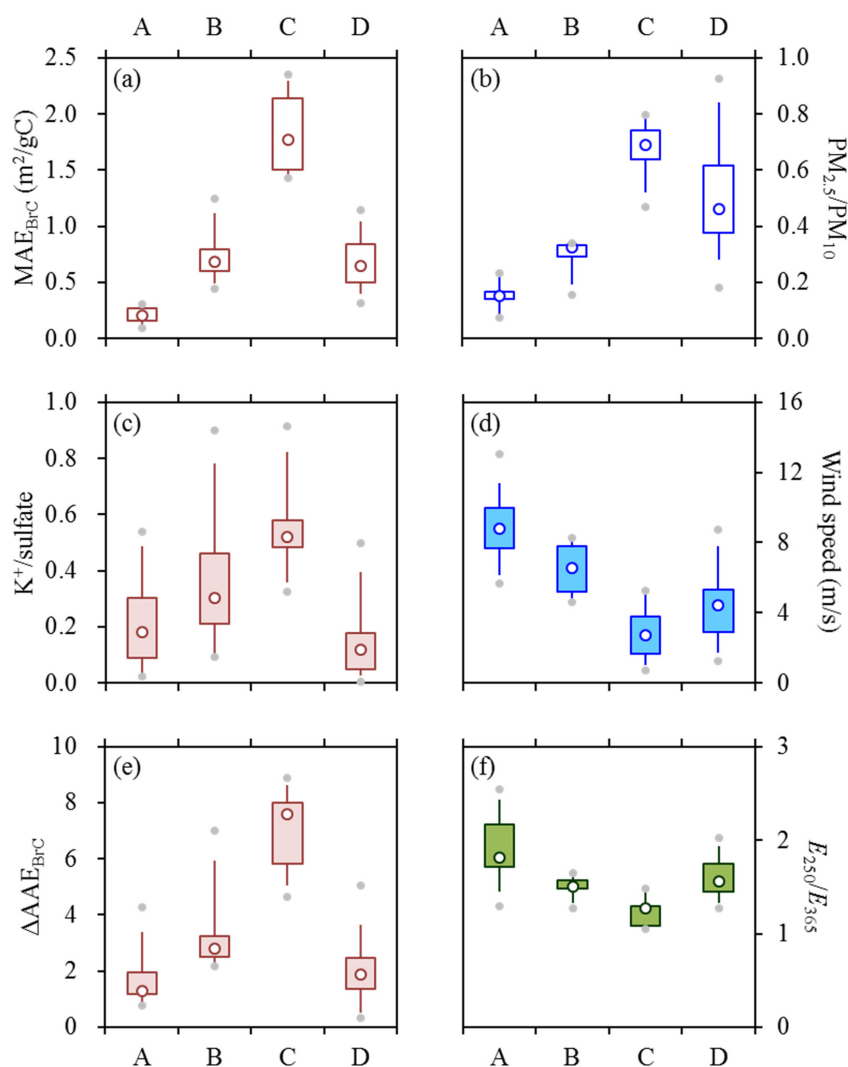


308 reduced K^+ /sulfate could be translated into little impact of open burning. The clear association
309 between K^+ /sulfate and agricultural fires was also supported by the contrasting fire hotspot detection
310 results between periods with different K^+ /sulfate levels (Figure S4). Then based on a synthesis of
311 $PM_{2.5}/PM_{10}$, wind speed and K^+ /sulfate, it was concluded that the first group of samples were subject
312 to strong influences of dusts but insignificant impacts from agricultural fires. Contrasting to the first
313 group, the second group of samples ($N = 8$, case C in Figure 5) accompanied with the higher-end
314 MAE_{BrC} values (1.75–3.23 m^2/gC) showed quite different features (Figures 5a–5d), including higher
315 $PM_{2.5}/PM_{10}$ (0.69), lower wind speeds (2.71 m/s) and larger K^+ /sulfate (0.52). These signatures
316 suggested strong influences of agricultural fires but little impact of dusts. In the following
317 discussions, the first and second groups of samples will be referred to as dust-impacted and fire-
318 impacted ones, respectively.

319 After excluding the two distinct groups discussed above, the remaining samples showed
320 moderate MAE_{BrC} levels but considerable variations in other signatures. Some of the samples ($N =$
321 7, the third group; case B in Figure 5) were heavily polluted in PM_{10} (~140–305 $\mu g/m^3$) and
322 exhibited mixed features of the dust-impacted and fire-impacted samples (Figures 5b–5d), with the
323 median values of all the three signatures (i.e., $PM_{2.5}/PM_{10}$, wind speed and K^+ /sulfate) falling in-
324 between the first two groups. The other samples ($N = 35$, the fourth group; case D in Figure 5) had
325 substantially lower PM_{10} (averaging $53.45 \pm 29.78 \mu g/m^3$) and were characterized by pretty low
326 K^+ /sulfate (0.12), and moderate levels of both $PM_{2.5}/PM_{10}$ (0.46) and wind speeds (4.44 m/s). It
327 appeared that neither agricultural fires nor dusts exerted a strong influence on these samples, which
328 could thus be used to represent the typical conditions of the spring campaign. In the following
329 discussions, the third and fourth groups of samples will be termed fire&dust-impacted and typical



330 ones, respectively.



331

332 **Figure 5.** Variations of (a) MAE_{BrC}, (b) PM_{2.5}/PM₁₀, (c) K⁺/sulfate, (d) wind speeds, (e) ΔAAE_{BrC}
 333 and (f) E₂₅₀/E₃₆₅ across cases of A–D, which correspond to the dust-impacted, fire&dust-impacted,
 334 fire-impacted and typical samples, respectively. Lower and upper box bounds indicate the 25th and
 335 75th percentiles, the whiskers below and above the box indicate the 5th and 95th percentiles, the solid
 336 circles below and above the box indicate the minimum and maximum, and the open circle within
 337 the box marks the median.

338

The identification of the four groups was also supported by the spectral measurement results



339 from the methanol extracts of filter samples. It has been commonly recognized that light absorption
340 by brown carbon exhibits stronger wavelength (λ) dependence compared to black carbon, leading
341 to larger absorption Ångström exponent of BrC (AAE_{BrC}). Using the solution-based light absorption
342 spectra, AAE_{BrC} could be determined as the slope derived from the linear regression of $\ln[(b_{abs})_{MS-}$
343 $BrC]$ against $\ln(\lambda)$. As shown by our previous study in Northeast China, when the agricultural fire
344 impact was insignificant, $\ln[(b_{abs})_{MS-BrC}]$ exhibited a strong linear correlation with $\ln(\lambda)$ and thus
345 AAE_{BrC} could be readily determined over a relatively wide wavelength range of 310–460 nm
346 (Cheng et al., 2023). During agricultural fire episodes, however, the dependence of $\ln[(b_{abs})_{MS-BrC}]$
347 on $\ln(\lambda)$ tended to be non-linear, since the fire-emitted chromophores could result in a distinct
348 absorption peak at ~ 365 nm (Cheng et al., 2023). The non-linear correlation between $\ln[(b_{abs})_{MS-BrC}]$
349 and $\ln(\lambda)$ was also evident for the fire-impacted samples in this study. To quantitatively describe the
350 non-linearity, we calculated the difference in AAE_{BrC} over two wavelength ranges (i.e., 410–460
351 and 310–360 nm) and defined this difference as ΔAAE_{BrC} (Figure S5). As shown in Figure 5e,
352 different groups of samples indeed showed considerable discrepancies in ΔAAE_{BrC} . For example,
353 the ΔAAE_{BrC} levels were found to be highest for the fire-impacted samples (7.60 in terms of median
354 value), moderate for the fire&dust-impacted samples (2.81), and lowest for the dust-impacted
355 samples (1.30). In addition, ΔAAE_{BrC} differed significantly between the fire&dust-impacted and
356 typical samples (2.81 vs. 1.86), demonstrating the necessity for further distinguishing the two groups
357 of samples despite their comparable MAE_{BrC} levels.

358 Another diagnostic parameter that could be derived from the light absorption spectra of MSOC
359 was the ratio of $(b_{abs})_{MS-BrC}$ at 250 nm to that at 365 nm, which was usually termed E_{250}/E_{365} . This
360 ratio was proposed as an indicator for the chemical properties of the dissolved organics, e.g., higher



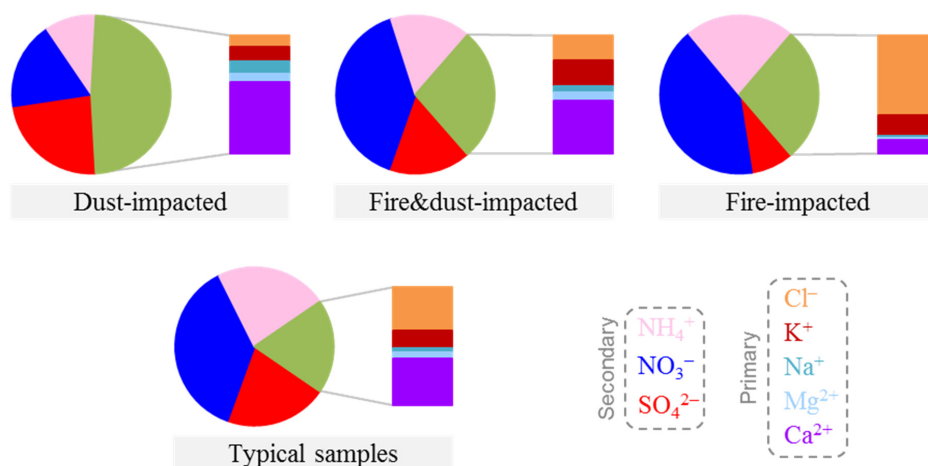
361 E_{250}/E_{365} typically indicated smaller molecular sizes and lower aromaticity (Duarte et al., 2005;
362 Chen et al., 2019). In this study, E_{250}/E_{365} exhibited a clear decreasing trend across the dust-impacted,
363 fire&dust-impacted and fire-impacted samples (Figure 5f), i.e., with increasing impacts of
364 agricultural fires. On one hand, this trend confirmed the heterogeneity of different groups of samples,
365 from the perspective of the chemical properties of MSOC. On the other hand, this trend suggested
366 that compared to those associated with dusts, the fire-emitted organic compounds were likely
367 characterized by higher molecular weights and higher aromatic contents, which should be highly
368 responsible for the strong light absorption capacities of the fire-impacted samples.

369 3.3 Comparison of inorganic species across different episodes

370 Figure 6 compares the compositions of water-soluble inorganic ions among different groups of
371 samples. The ions were broadly separated into secondary species (i.e., sulfate, nitrate and
372 ammonium) and primary components (i.e., Cl^- , K^+ , Na^+ , Mg^{2+} and Ca^{2+}). Based on the ion
373 concentrations averaged for each group, the dust-impacted samples were found to differ
374 significantly from the other ones in three aspects, including higher fraction of primary species in
375 total ions (48% vs. < 30%), larger contribution of Ca^{2+} to primary ions (61% vs. < 45%) and higher
376 ratio of sulfate to nitrate (1.31 vs. < 0.6). The fire-impacted samples also exhibited several distinct
377 features, including the dominant contribution of Cl^- to primary ions (68% vs. < 40% for the other
378 groups) and the remarkably high ratio of nitrate to sulfate (4.73). Actually, the fraction of Ca^{2+} in
379 primary ions showed a clear decreasing trend across the dust-impacted, fire&dust-impacted and fire-
380 impacted episodes (from 61% to 12%), while an opposite trend was observed for the fraction of Cl^-
381 (from 10% to 68%). These patterns were not surprising, since Ca^{2+} and Cl^- had been commonly
382 identified in dust and agricultural fire emissions, respectively (Bi et al., 2019). One may argue that



383 Cl^- should be used in Section 3.2 for the separation of samples into different groups. Besides open
 384 burning, however, there existed other important sources for Cl^- (Bi et al., 2019), e.g., coal
 385 combustion. Given the relatively low temperatures during the spring campaign (averaging 8.5 °C
 386 and around 0 °C for ~25% of the samples), coal combustion was expected to contribute considerably.
 387 The prevalence of coal combustion emissions was in line with the largely comparable Cl^- to sulfate
 388 ratios observed for the samples after excluding the fire-impacted ones (Figure S6). The substantial
 389 contribution of Cl^- to primary ions (37%) determined for the typical samples also confirmed the
 390 substantial contribution of coal combustion. The discussions above indicated that the relative
 391 abundances of Cl^- could be used to isolate the periods with strong influences of fires, but were less
 392 capable of identifying other episodes (e.g., the fire&dust-impacted samples).



393
 394 **Figure 6.** Comparison of water-soluble ion compositions across the dust-impacted, fire&dust-
 395 impacted, fire-impacted and typical samples. In each pie chart, the unlabeled fraction indicates the
 396 sum of the primary ions.

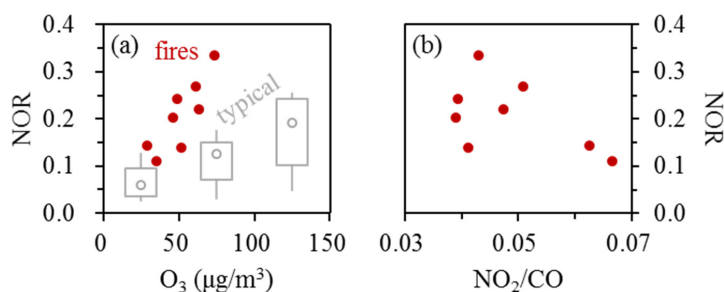
397 The fire-impacted samples showed significantly higher relative abundance of nitrate compared
 398 to sulfate (Figure 6), likely pointing to enhanced formation of nitrate under strong influences of
 399 agricultural fire emissions. This inference was supported by the comparison of nitrogen oxidation



400 ratios (NOR) among different episodes (Figure 7a). For the typical conditions of spring (i.e., as
401 reflected by the typical samples), NOR generally exhibited an increasing trend as ozone became
402 higher (Figure 7a), showing larger values (accompanied with elevated ozone) during the daytime
403 (Figure S7). The positive dependence of NOR on ozone held as well for the fire-impacted samples,
404 all of which occurred at night. However, it is noteworthy that the fire-impacted samples generally
405 showed higher NOR values than the typical ones with comparable ozone levels. Although drivers
406 for the increased NOR remained unclear based on the available observations, it was hypothesized
407 that some distinct dark-reactions occurred in the agricultural fire plumes and ultimately enhanced
408 the nitrate formation. As suggested by results from the laboratory-generated biomass burning smoke
409 (Ahern et al., 2018) and ambient open-burning plume (Decker et al., 2019), such nocturnal processes
410 may include the production of NO_3 radicals and N_2O_5 , the heterogeneous transformation of N_2O_5
411 into nitrate (e.g., on the surface of the abundant biomass-burning particles), and the reaction of NO_3
412 radicals with biomass burning VOCs (which could result in complex products including nitrate). In
413 addition, for the fire-impacted samples, the conditions with relatively low ratios of NO_2 to CO
414 (NO_2/CO) seemed more favorable for the enhancement of NOR (Figure 7b). Results from the
415 laboratory measurement and satellite-based observation of biomass burning smoke suggested that
416 decreased NO_2/CO ratios were typically associated with more smoldering combustion, which would
417 emit large amounts of CO but was less favorable for NO_2 production (van der Velde et al., 2021;
418 Anderson et al., 2023). Thus the association between elevated NOR and reduced NO_2/CO likely
419 indicated that the low-efficiency fires were more favorable for the nocturnal nitrate formation. It
420 should also be noted that NOR exhibited considerable sample-by-sample variations at similarly low
421 levels of NO_2/CO (e.g., below ~ 0.05). A possible explanation was that the NO_2/CO values presented



422 in Figure 7b were the averages of the time-resolved results measured during the fire episodes, and
 423 thus were only rough indicators for the overall burning conditions. Another likely cause was that
 424 besides the combustion efficiency, there existed other influencing factors for NOR in the fire plumes.
 425 The detailed chemical mechanisms for the fire-induced enhancement in nocturnal NOR, including
 426 the roles of combustion efficiencies (which are expected to influence the profiles of the fire
 427 emissions), merit further investigations.



428

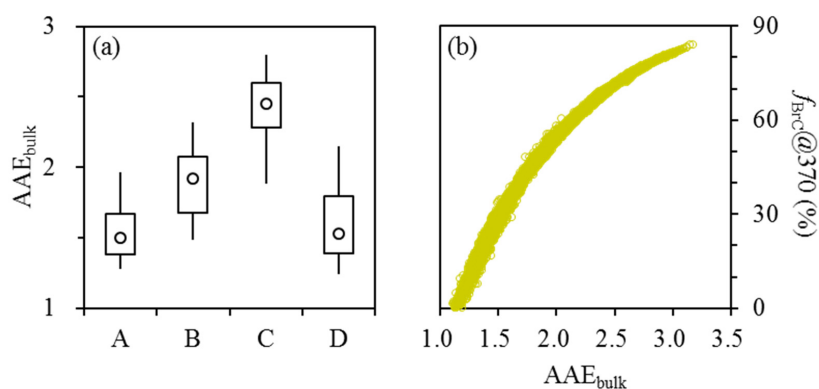
429 **Figure 7.** Dependences of NOR on (a) ozone (as shown by the solid circles) and (b) NO₂/CO for
 430 the fire-impacted samples. In (a), results from the typical samples are also presented for comparison,
 431 as shown by the overlaying box plot. Here the typical samples were divided into three subgroups
 432 with ozone concentrations of below 50, 50–100 and 100–150 µg/m³, respectively. NOR was
 433 calculated as n-nitrate/(n-nitrate + n-NO₂), where “n” indicates the molar concentration. To align
 434 with the off-line nitrate, the time-resolved NO₂ were first averaged for the filter sampling segments
 435 and then used for the NOR calculation.

436 3.4 Impacts of open burning and secondary formation on the BrC-related signatures

437 As discussed in Section 3.2, agricultural fire emissions exhibited pronounced influences on
 438 MAE_{BrC}, ΔAAE_{BrC} and E₂₅₀/E₃₆₅, by enhancing the light absorption capacity of bulk BrC, emitting
 439 distinct chromophores with a characteristic absorption peak at ~365 nm, and producing organic
 440 compounds with relatively high molecular weights and aromatic contents, respectively. Besides
 441 these signatures, the wavelength dependence of aerosol absorption (AAE_{bulk}) and the relative
 442 importance of BrC absorption (primarily investigated at 370 nm as f_{BrC@370}) were also



443 significantly impacted by the fire emissions. Here $f_{\text{BrC}@370}$ was calculated as the ratio of
 444 $(b_{\text{abs}})_{\text{BrC}@370}$ to $(b_{\text{abs}})_{@370}$, with $(b_{\text{abs}})_{\text{BrC}@370}$ determined by Equation (1) using an AAE_{BC} of
 445 1.10 and $(b_{\text{abs}})_{@370}$ obtained by applying the C^* values in Table 1 to the AE33 results. As can be
 446 seen from Figures 8a and S8, both AAE_{bulk} and $f_{\text{BrC}@370}$ showed clear increasing trends as the fire
 447 impacts became stronger. For example, the median AAE_{bulk} increased substantially across the dust-
 448 impacted, fire&dust-impacted and fire-impacted samples (from 1.50 to 2.45). Meanwhile, the
 449 median $f_{\text{BrC}@370}$ was enhanced by 2.5 folds, from 28% to 70%. These patterns were not surprising,
 450 given the significance of biomass burning as a BrC source (Washenfelder et al., 2015) and the fact
 451 that the light absorption by BrC typically shows stronger wavelength dependence, i.e., increases
 452 more sharply towards shorter wavelengths, compared to BC. In addition, it appeared that AAE_{bulk}
 453 could be used an alternative estimate for the BrC contribution to aerosol absorption, since a
 454 consistent dependence of $f_{\text{BrC}@370}$ on AAE_{bulk} was observed for different episodes, regardless of
 455 the variations of aerosol sources (Figure 8b).

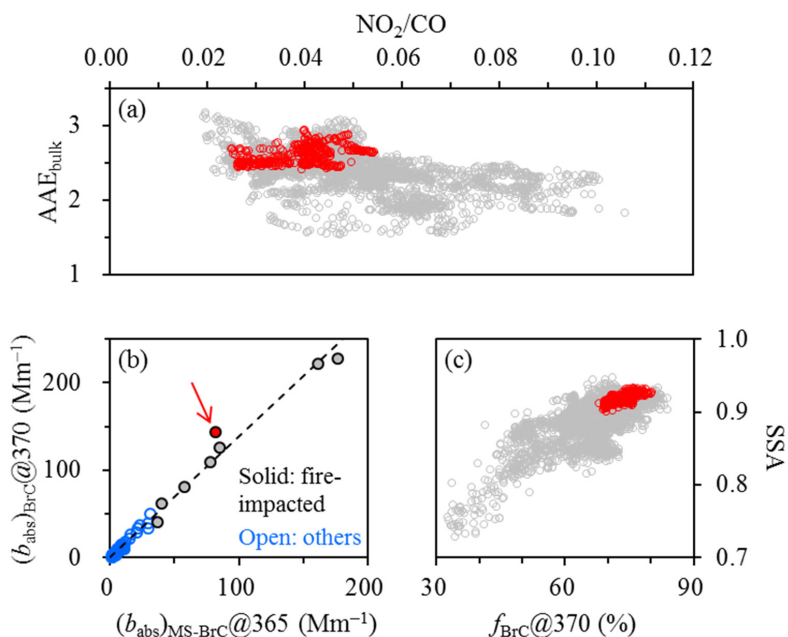


456

457 **Figure 8. (a)** Variation of AAE_{bulk} across cases of A–D, which correspond to the dust-impacted,
 458 fire&dust-impacted, fire-impacted and typical samples, respectively. **(b)** Relationship between
 459 $f_{\text{BrC}@370}$ and AAE_{bulk} (results from different cases were not distinguished). Time-resolved AAE_{bulk}
 460 and $f_{\text{BrC}@370}$ were first extracted for the filter sampling segments and then used for the comparisons.



461 For the agricultural fire episodes, AAE_{bulk} generally exhibited a negative dependence on the
462 ratio of NO_2 to CO (NO_2/CO), e.g., elevated AAE_{bulk} usually occurred at relatively low NO_2/CO
463 levels (Figure 9a). Recalling the association between decreased NO_2/CO and more smoldering
464 combustion, the low-efficiency fire emissions were presumably an important driver for the increase
465 of AAE_{bulk} , i.e., the enhancement of $f_{\text{BrC}@370}$. In addition, one fire-impacted sample (collected on
466 the night of April 15, 2023) was noticed to exhibit relatively large discrepancy between the AE33-
467 based $(b_{\text{abs}})_{\text{BrC}@370}$ and the solution-based $(b_{\text{abs}})_{\text{MS-BrC}@365}$ (Figure 9b), likely suggesting an
468 increase in the fraction of methanol-insoluble species in total OC. This sample was also
469 characterized by relatively low levels of NO_2/CO , pointing to the prevalence of low-efficiency fires
470 for the sampling period and the potential contribution of such fires to methanol-insoluble OC. This
471 inference was partially supported by association of reduced E_{250}/E_{365} with decreased NO_2/CO
472 (Figure S9), which indicated that the low-efficiency fires favored the emissions of organic
473 compounds with relatively high molecular weights and aromatic contents. It is also noteworthy that
474 although the BrC particles from agricultural fires, especially those with low efficiencies, contributed
475 considerably to aerosol absorption in the ultraviolet wavelength range, they likely appeared more
476 scattering at 870 nm, the wavelength for the PAX-based SSA determination. For example, SSA
477 exhibited a clear increasing trend as $f_{\text{BrC}@370}$ became higher (Figure 9c), indicating that the BrC
478 particles exerted limited impact on the aerosol absorption at 870 nm.



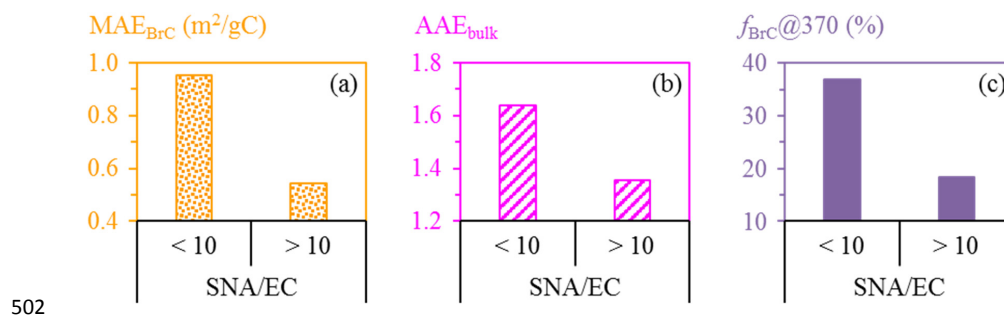
479

480 **Figure 9.** (a) Relationship between time-resolved AAE_{bulk} and NO_2/CO for the fire episodes. (b)
 481 Comparison of the AE33-based $(b_{abs})_{BrC}@370$ and the filter-based $(b_{abs})_{MS-BrC}@365$. (c)
 482 Relationship between time-resolved SSA and $f_{BrC}@370$ for the fire episodes. In (b), results from the
 483 fire-impacted and other samples were shown separately, while the dashed line indicates the linear
 484 regression result determined based on all of the spring samples. The sample collected on the night
 485 of April 15, 2023 was indicated by the arrow. In (a) and (c), results during the collection period of
 486 this specific sample were also highlighted, as shown by the red data points.

487 SOA formation was identified as another influencing factor for BrC. Here we focused on the
 488 typical samples to minimize the impacts of agricultural fires and dusts. Although SOA tracer was
 489 not directly measured in this study, the ratio of SNA (i.e., the sum of secondary inorganic ions
 490 including sulfate, nitrate and ammonium) to EC could be used as an indirect indicator for the
 491 significance of SOA formation. The effectiveness of this indicator was supported by the concurrent
 492 enhancements in SNA and SOA repeatedly observed in Harbin (Cheng et al., 2021; Cheng and He,
 493 2026). As shown in Figure 10a, MAE_{BrC} dropped considerably once the SNA to EC ratio (SNA/EC)
 494 exceeded 10, with the median MAE_{BrC} almost halved (from 0.95 to 0.51 m^2/gC). It appeared that



495 the bulk BrC tended to be less absorbing as more SOA was produced. This pattern was with
 496 expectation, since SOA typically had weaker light absorption capacities than primary organic
 497 matters (Kumar et al., 2018; Cappa et al., 2020). Similar to MAE_{BrC} , AAE_{bulk} and $f_{BrC@370}$ were
 498 also substantially lower for the SNA/EC range of above 10 (Figures 10b–c), with their median
 499 values decreasing from 1.64 to 1.35 and from 37% to 18%, respectively. The discussions above
 500 suggested that SOA formation could reduce the MAE of bulk BrC and the influence of BrC on the
 501 total light absorption of aerosol.



502
 503 **Figure 10.** Comparisons of (a) MAE_{BrC} , (b) AAE_{bulk} and (c) $f_{BrC@370}$ with SNA/EC ratios of below
 504 and above 10, for the typical samples. Time-resolved AAE_{bulk} and $f_{BrC@370}$ were first extracted for
 505 the filter sampling segments and then used for the comparisons. Only the median values are shown
 506 here. Refer to Figure S10 for detailed comparisons.

507 3.5 Evidences for considerable light absorption enhancement of black carbon

508 Similar to MAE_{BrC} , the mass absorption efficiency of BC (MAE_{BC}) was calculated as the ratio
 509 of the PAX-based (b_{abs})@870 to EC, and the results were specified as $MAE_{BC@870}$. A consensus
 510 had been reached that the mass absorption efficiency of uncoated black carbon should be at least 5
 511 m^2/g at 550 nm (Bond et al., 2013; Petzold et al., 2013). This lower limit, which was suggested as a
 512 fundamental physical property of black carbon, could be converted to a threshold value of $3.02 m^2/g$
 513 at 870 nm (using an AAE_{BC} of 1.1). For the dust-impacted, fire&dust-impacted and fire-impacted

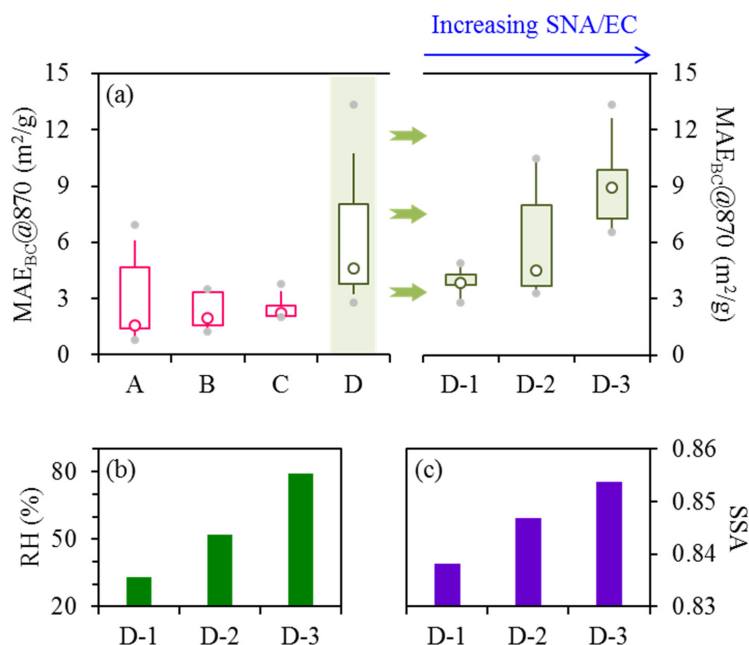


514 episodes, the majority (~55–90%) of the samples showed $MAE_{BC@870}$ values smaller than 3.02
515 m^2/g , and the median $MAE_{BC@870}$ were only 1.59, 1.95 and 2.25 m^2/g , respectively (Figure 11a).
516 Such unrealistically low $MAE_{BC@870}$ could hardly be explained by uncertainties in the PAX-based
517 absorption measurement but pointed to overestimation of black carbon mass by EC. In thermal-
518 optical analysis, the interfering components for EC determination may include carbonate and brown
519 carbon, which were closely associated with dusts and biomass burning, respectively. For example,
520 previous studies suggested that calcium carbonate ($CaCO_3$) did not completely decompose at 650 °C
521 when heated in an inert atmosphere (Karanasidou et al., 2011), and tar balls from open burning could
522 retain ~30% of their volumes at 600 °C (Adachi et al., 2017; Sedlacek III et al., 2018). For the
523 IMPROVE-A temperature protocol used in this study, the peak temperature of the inert mode was
524 580 °C. Thus when the dust and/or agricultural fire impacts were significant, it was very likely that
525 a fraction of the carbonate and/or brown carbon could slip into the oxidizing mode of the analysis
526 and then be misidentified as EC. It is also noteworthy that among the fire episodes, the events with
527 unrealistically low $MAE_{BC@870}$ values (e.g., around 2 m^2/g) typically showed relatively smaller
528 NO_2/CO (Figure S11), suggesting the low-efficiency fires as an important source for the interfering
529 species in thermal-optical EC measurement.

530 The overestimation of EC mass became non-evident for the typical samples, as indicated by
531 their $MAE_{BC@870}$ levels which stayed above ~3 m^2/g (Figure 11a). In addition, the $MAE_{BC@870}$
532 values were found to exhibit significant sample-by-sample variations. In general, MAE_{BC} is strongly
533 influenced by the particle mixing state, with relatively low levels for uncoated black carbon. As BC
534 is internally mixed with (i.e., coated by) non-refractory components (e.g., sulfate), MAE_{BC} typically
535 tends to increase to varying degrees, and the specific magnitude depends on many factors such as



536 the complex refractive index of the coating materials (Liu et al., 2014) and the detailed particle
537 morphology (e.g., the position of BC within the coating materials; Huang et al., 2024). In this study,
538 the variations of $MAE_{BC@870}$ were closely related to the changes in SNA/EC. As shown in Figure
539 11a, $MAE_{BC@870}$ showed a clear increasing trend across the SNA/EC ranges of below 5, 5–10 and
540 above 10, with the median $MAE_{BC@870}$ increasing from 3.83 to 4.53 m^2/g and finally reaching
541 8.94 m^2/g . SNA/EC was not only a direct measure of secondary inorganic aerosol production but
542 also an indirect indicator for SOA formation (as discussed in Section 3.4). Thus the positive
543 dependence of $MAE_{BC@870}$ on SNA/EC was presumably driven by secondary aerosols, which
544 could effectively enhance BC absorption by internal mixing. Using the median $MAE_{BC@870}$
545 determined for the SNA/EC range of below 5 as the reference, the light absorption enhancement
546 factors were estimated to be 1.18 and 2.33 for the SNA/EC ranges of 5–10 and above 10,
547 respectively. Given that RH increased substantially across the three SNA/EC ranges (Figure 11b),
548 heterogeneous reactions involving aerosol water was inferred to be highly favorable for the
549 secondary aerosol production and BC absorption enhancement. In addition, SSA elevated slightly
550 with increasing SNA/EC (Figure 11c), indicating that the particles tended to be more scattering as
551 the secondary aerosol formation was enhanced.



552

553 **Figure 11.** (a) Variation of $MAE_{BC}@870$ across cases of A–D, which correspond to the dust-
 554 impacted, fire&dust-impacted, fire-impacted and typical samples, respectively. Results from the
 555 typical samples were further divided into three subgroups, i.e., D-1 to D-3 which had SNA/EC ratios
 556 of below 5, 5–10 and above 10, respectively. Comparisons of (b) RH and (c) SSA across D-1 to D-
 557 3 (only the median values are shown).

558 4. Conclusions

559 During a spring period with dramatic variations of $PM_{2.5}$ sources, PAX, AE33 and off-line
 560 observations were integrated to explore the aerosol optical properties in a representative megacity
 561 in Northeast China. PAX was used as the reference method to constrain the multiple scattering effect
 562 in the AE33-based absorption measurement. The correction factor retrieved (C^*) was found to
 563 depend positively on SSA whereas their relationship was non-linear. To enhance the relevance of
 564 the time-resolved correction factors to future studies, we determined the median C^* for various SSA
 565 bins, which covered the typical SSA ranges encountered in ambient conditions. After applying the
 566 SSA-dependent C^* , the corrected AE33 results were in reasonable agreement with the PAX-based



567 absorption coefficients. We also observed considerable differences but strong correlations between
568 the AE33 and off-line absorption measurements. For the absorption coefficient of bulk aerosol, the
569 carbon analyzer reported higher values than AE33, with $(b_{\text{abs}})^{\#}@632$ approximately 50% larger than
570 $(b_{\text{abs}})^{*}@632$. This discrepancy was primarily attributed to the different filter materials used by the
571 two instruments. In addition, for the absorption coefficient of brown carbon, results from the AE33
572 were ~ 1.4 times higher than those obtained by the spectrophotometric measurement of BrC
573 solutions. A likely cause for this discrepancy was the difference in the states of the measured BrC
574 (particulate vs. dissolved), while another contributor was inferred to be the chromophores insoluble
575 in methanol, which were not accounted for in the solution-based approach.

576 After elucidating the relationships between the optical parameters determined by different
577 approaches, we identified three types of episodes (i.e., dust-impacted, fire&dust-impacted, and fire-
578 impacted) and the typical periods for the spring campaign. The classification was based on a
579 synthesis of various signatures, including the MAE of BrC, the $\text{PM}_{2.5}$ to PM_{10} ratio, wind speed and
580 the K^+ to sulfate ratio. The classification results were also supported by another two signatures,
581 $\Delta\text{AAE}_{\text{BrC}}$ and E_{250}/E_{365} .

582 By comparing results from different periods, we highlighted the strong impacts of agricultural
583 fire emissions on BrC. For example, the fires effectively enhanced the light absorption capacity of
584 bulk BrC, emitted distinct chromophores with a characteristic absorption peak at ~ 365 nm (as
585 indicated by the increased $\Delta\text{AAE}_{\text{BrC}}$), and produced organic compounds with relatively high
586 molecular weights and aromatic contents (as indicated by the decreased E_{250}/E_{365}). In addition, the
587 agricultural fires, especially those having relatively low combustion efficiencies, effectively
588 increased the AAE of bulk aerosol and the BrC contribution to total absorption in the ultraviolet



589 wavelength range.

590 We also unfolded the responses of BrC and BC optical properties to secondary aerosol
591 formation. For typical samples, i.e., those without significant impacts from agricultural fires or dusts,
592 we found that with the enhancement of secondary aerosol, the bulk BrC appeared less absorbing
593 and consequently, the BrC influences on the light absorption of total aerosol became weaker, as
594 reflected by the concurrent decreases in AAE_{bulk} and $f_{\text{BrC}@370}$. However, there was observational
595 evidence pointing to a considerable increase in the MAE of BC driven by secondary aerosol
596 production, which could be translated into light absorption enhancement (E_{abs}) factors of up to ~ 2.3 .

597 Finally, our results revealed the distinctiveness of the low-efficiency agricultural fire emissions
598 in Northeast China. In addition to emitting unique organic matters (e.g., those with relatively high
599 molecular weights and aromatic contents, and those strongly interfering thermal-optical EC
600 determination), and effectively enhancing the BrC impacts on total aerosol light absorption, such
601 fires could also promote nocturnal nitrate formation, likely due to some distinct dark-reactions. We
602 suggest that the low-efficiency fires merit further investigations, e.g., for the emissions of gaseous
603 and particulate species, the plume evolution, and the interactions of the fire emissions with other
604 anthropogenic pollutants.

605 **Data availability.** Data described in this manuscript can be accessed at
606 <https://doi.org/10.5281/zenodo.18898994> (Cheng, 2026).

607 **Author contributions.** YC and JL designed the study and prepared the paper, with inputs from all
608 the co-authors. XC, YG, YZ and ZZ carried out the experiments. KH validated the results and
609 supervised the study.

610 **Competing interests.** The authors declare that they have no conflict of interest.



611 **Disclaimer.** Publisher's note: Copernicus Publications remains neutral with regard to jurisdictional
612 claims made in the text, published maps, institutional affiliations, or any other geographical
613 representation in this paper. While Copernicus Publications makes every effort to include
614 appropriate place names, the final responsibility lies with the authors.

615 **Acknowledgments.** The authors thank Dr. Yue-mei Han at Institute of Earth Environment, Chinese
616 Academy of Sciences for the help in sample analysis.

617 **Financial support.** This research has been supported by the National Natural Science Foundation
618 of China (42222706 and 22188102), the Natural Science Foundation of Heilongjiang Province
619 (YQ2024D011), and the Fundamental Research Funds for the Central Universities.

620 **References**

621 Adachi, K., Sedlacek III, A. J., Kleinman, L., Chand, D., Hubbe, J. M., and Buseck, P. R.: Volume
622 changes upon heating of aerosol particles from biomass burning using transmission electron
623 microscopy, *Aerosol Sci. Technol.*, 52, 46–56,
624 <https://doi.org/10.1080/02786826.2017.1373181>, 2017.

625 Ahern, A. T., Goldberger, L., Jahl, L., Thornton, J., and Sullivan, R. C.: Production of N₂O₅ and
626 ClNO₂ through nocturnal processing of biomass-burning aerosol, *Environ. Sci. Technol.*, 52,
627 550–559, <https://doi.org/10.1021/acs.est.7b04386>, 2018.

628 Anderson, L. D., Dix, B., Schnell, J., Yokelson, R., Veeffkind, J. P., Ahmadov, R., and de Gouw, J.:
629 Analyzing the impact of evolving combustion conditions on the composition of wildfire
630 emissions using satellite data, *Geophys. Res. Lett.*, 50, e2023GL105811,
631 <https://doi.org/10.1029/2023GL105811>, 2023.

632 Andreae, M. O., and Gelencsér, A.: Black carbon or brown carbon? The nature of light-absorbing
633 carbonaceous aerosols, *Atmos. Chem. Phys.*, 6, 3131–3148, <https://doi.org/10.5194/acp-6-3131-2006>, 2006.

635 Atwi, K., Cheng, Z. Z., El Hajj, O., Perrie, C., and Saleh, R.: A dominant contribution to light
636 absorption by methanol-insoluble brown carbon produced in the combustion of biomass fuels



- 637 typically consumed in wildland fires in the United States, *Environ. Sci. Atmos.*, 2, 182–191,
638 <https://doi.org/10.1039/d1ea00065a>, 2022.
- 639 Bi, X., Dai, Q., Wu, J., Zhang, Q., Zhang, W., Luo, R., Cheng, Y., Zhang, J., Wang, L., Yu, Z., Zhang,
640 Y., Tian, Y., and Feng, Y.: Characteristics of the main primary source profiles of particulate
641 matter across China from 1987 to 2017, *Atmos. Chem. Phys.*, 19, 3223–3243,
642 <https://doi.org/10.5194/acp-19-3223-2019>, 2019.
- 643 Bond, T. C., Doherty, S. J., Fahey, D. W., Forster, P. M., Berntsen, T., DeAngelo, B. J., Flanner, M.
644 G., Ghan, S., Kärcher, B., Koch, D., Kinne, S., Kondo, Y., Quinn, P. K., Sarofim, M. C., Schultz,
645 M. G., Schulz, M., Venkataraman, C., Zhang, H., Zhang, S., Bellouin, N., Guttikunda, S. K.,
646 Hopke, P. K., Jacobson, M. Z., Kaiser, J. W., Klimont, Z., Lohmann, U., Schwarz, J. P., Shindell,
647 D., Storelvmo, T., Warren, S. G., and Zender, C. S.: Bounding the role of black carbon in the
648 climate system: a scientific assessment, *J. Geophys. Res.*, 118, 5380–5552,
649 <https://doi.org/10.1002/jgrd.50171>, 2013.
- 650 Cappa, C. D., Lim, C. Y., Hagan, D. H., Coggon, M., Koss, A., Sekimoto, K., de Gouw, J., Onasch,
651 T. B., Warneke, C., and Kroll, J. H.: Biomass-burning-derived particles from a wide variety of
652 fuels – Part 2: Effects of photochemical aging on particle optical and chemical properties,
653 *Atmos. Chem. Phys.*, 20, 8511–8532, <https://doi.org/10.5194/acp-20-8511-2020>, 2020.
- 654 Chang, X., Zhao, B., Zheng, H. T., Wang, S. X., Cai, S. Y., Guo, F. Q., Gui, P., Huang, G. H., Wu,
655 D., Han, L. C., Xing, J., Man, H. Y., Hu, R. L., Liang, C. R., Xu, Q. C., Qiu, X. H., Ding, D.,
656 Liu, K. Y., Han, R., Robinson, A. L., and Donahue, N. M.: Full-volatility emission framework
657 corrects missing and underestimated secondary organic aerosol sources, *One Earth*, 5, 403–
658 412, 2022.
- 659 Chen, Q. C., Mu, Z., Song, W. H., Wang, Y. Q., Yang, Z. H., Zhang, L. X., and Zhang, Y. L.: Size-
660 resolved characterization of the chromophores in atmospheric particulate matter from a typical
661 coal-burning city in China, *J. Geophys. Res. Atmos.*, 124, 10546–10563,
662 <https://doi.org/10.1029/2019JD031149>, 2019.
- 663 Chen, X. Y., Ching, J., Wu, F., Matsui, H., Jacobson, M. Z., Zhang, F., Wang, Y. Y., Zhang, Z. X.,
664 Liu, D. T., Zhu, S. P., Rudich, Y., Shi, Z. B., Yoo, H., Jeon, K. J., and Li, W. J.: Locating the
665 missing absorption enhancement due to multi-core black carbon aerosols, *Nat. Commun.*, 16,
666 10187, <https://doi.org/10.1038/s41467-025-65079-2>, 2025.



- 667 Cheng, Y.: Optical properties of carbonaceous aerosols modulated by source variations of spring
668 haze, Zenodo [Data set], <https://doi.org/10.5281/zenodo.18898994>, 2026.
- 669 Cheng, Y., Cao, X. B., Liu, J. M., Zhong, Y. J., Yu, Q. Q., Zhang, Q., and He, K. B.: Measurement
670 report: Diurnal variations of brown carbon during two distinct seasons in a megacity in
671 northeast China, *Atmos. Chem. Phys.*, 23, 6241–6253, [https://doi.org/10.5194/acp-23-6241-](https://doi.org/10.5194/acp-23-6241-2023)
672 2023, 2023.
- 673 Cheng, Y., and He, K. B.: Northeast China: an emerging hotspot of atmospheric sciences, *Sci. Bull.*,
674 71, 64–66, <https://doi.org/10.1016/j.scib.2025.06.023>, 2026.
- 675 Cheng, Y., Yu, Q., Liu, J., Cao, X., Zhong, Y., Du, Z., Liang, L., Geng, G., Ma, W., Qi, H., Zhang,
676 Q., and He, K.: Dramatic changes in Harbin aerosol during 2018–2020: the roles of open
677 burning policy and secondary aerosol formation, *Atmos. Chem. Phys.*, 21, 15199–15211,
678 <https://doi.org/10.5194/acp-21-15199-2021>, 2021.
- 679 Collaud Coen, M., Weingartner, E., Apituley, A., Ceburnis, D., Fierz-Schmidhauser, R., Flentje, H.,
680 Henzing, J. S., Jennings, S. G., Moerman, M., Petzold, A., Schmid, O., and Baltensperger, U.:
681 Minimizing light absorption measurement artifacts of the Aethalometer: evaluation of five
682 correction algorithms, *Atmos. Meas. Tech.*, 3, 457–474, [https://doi.org/10.5194/amt-3-457-](https://doi.org/10.5194/amt-3-457-2010)
683 2010, 2010.
- 684 Decker, Z. C. J., Zarzana, K. J., Coggon, M., Min, K. E., Pollack, I., Ryerson, T. B., Peischl, J.,
685 Edwards, P., Dubé, W. P., Markovic, M. Z., Roberts, J. M., Veres, P. R., Graus, M., Warneke,
686 C., de Gouw, J., Hatch, L. E., Barsanti, K. C., and Brown, S. S.: Nighttime chemical
687 transformation in biomass burning plumes: a box model analysis initialized with aircraft
688 observations, *Environ. Sci. Technol.*, 53, 2529–2538, <https://doi.org/10.1021/acs.est.8b05359>,
689 2019.
- 690 Drinovec, L., Močnik, G., Zotter, P., Prévôt, A. S. H., Ruckstuhl, C., Coz, E., Rupakheti, M., Sciare,
691 J., Müller, T., Wiedensohler, A., and Hansen, A. D. A.: The "dual-spot" Aethalometer: an
692 improved measurement of aerosol black carbon with real-time loading compensation, *Atmos.*
693 *Meas. Tech.*, 8, 1965–1979, <https://doi.org/10.5194/amt-8-1965-2015>, 2015.
- 694 Duarte, R. M. B. O., Pio, C. A., and Duarte, A. C.: Spectroscopic study of the water-soluble organic
695 matter isolated from atmospheric aerosols collected under different atmospheric conditions,
696 *Anal. Chim. Acta*, 530, 7–14, <https://doi.org/10.1016/j.aca.2004.08.049>, 2005.



- 697 Ferrero, L., Bernardoni, V., Santagostini, L., Cogliati, S., Soldan, F., Valentini, S., Massabò, D.,
698 Močnik, G., Gregorič, A., Rigler, M., Prati, P., Bigogno, A., Losi, N., Valli, G., Vecchi, R., and
699 Bolzacchini, E.: Consistent determination of the heating rate of light-absorbing aerosol using
700 wavelength- and time-dependent Aethalometer multiple-scattering correction, *Sci. Total*
701 *Environ.*, 791, 148277, <https://doi.org/10.1016/j.scitotenv.2021.148277>, 2021.
- 702 Gao, C. Y., Heald, C. L., Katich, J. M., Luo, G., and Yu, F. Q.: Remote aerosol simulated during the
703 Atmospheric Tomography (ATom) campaign and implications for aerosol lifetime, *J. Geophys.*
704 *Res. Atmos.*, 127, e2022JD036524, <https://doi.org/10.1029/2022JD036524>, 2022.
- 705 Geng, G. N., Liu, Y. X., Liu, Y., Liu, S. G., Cheng, J., Yan, L., Wu, N. N., Hu, H. W., Tong, D.,
706 Zheng, B., Yin, Z. C., He, K. B., and Zhang, Q.: Efficacy of China's clean air actions to tackle
707 PM_{2.5} pollution between 2013 and 2020, *Nat. Geosci.*, 17, 987–994,
708 <https://doi.org/10.1038/s41561-024-01540-z>, 2024.
- 709 Huang, X. F., Peng, Y., Wei, J., Peng, J. F., Lin, X. Y., Tang, M. X., Cheng, Y., Men, Z., Fang, T.,
710 Zhang, J. S., He, L. Y., Cao, L. M., Liu, C., Zhang, C. C., Mao, H. J., Seinfeld, J. H., and Wang,
711 Y.: Microphysical complexity of black carbon particles restricts their warming potential, *One*
712 *Earth*, 7, 136–145, <https://doi.org/10.1016/j.oneear.2023.12.004>, 2024.
- 713 Karanasiou, A., Diapouli, E., Cavalli, F., Eleftheriadis, K., Viana, M., Alastuey, A., Querol, X., and
714 Reche, C.: On the quantification of atmospheric carbonate carbon by thermal/optical analysis
715 protocols, *Atmos. Meas. Tech.*, 4, 2409–2419, <https://doi.org/10.5194/amt-4-2409-2011>, 2011.
- 716 Kumar, N. K., Corbin, J. C., Bruns, E. A., Massabó, D., Slowik, J. G., Drinovec, L., Močnik, G.,
717 Prati, P., Vlachou, A., Baltensperger, U., Gysel, M., El-Haddad, I., and Prévôt, A. S. H.:
718 Production of particulate brown carbon during atmospheric aging of residential wood-burning
719 emissions, *Atmos. Chem. Phys.*, 18, 17843–17861, [https://doi.org/10.5194/acp-18-17843-](https://doi.org/10.5194/acp-18-17843-2018)
720 2018, 2018.
- 721 Lack, D. A. and Langridge, J. M.: On the attribution of black and brown carbon light absorption
722 using the Ångström exponent, *Atmos. Chem. Phys.*, 13, 10535–10543,
723 <https://doi.org/10.5194/acp-13-10535-2013>, 2013.
- 724 Lambe, A. T., Cappa, C. D., Massoli, P., Onasch, T. B., Forestieri, S. D., Martin, A. T., Cummings,
725 M. J., Croasdale, D. R., Brune, W. H., Worsnop, D. R., and Davidovits, P.: Relationship



- 726 between oxidation level and optical properties of secondary organic aerosol, *Environ. Sci.*
727 *Technol.*, 47, 6349–6357, <https://doi.org/10.1021/es401043j>, 2013.
- 728 Laskin, A., Laskin, J., and Nizkorodov, S. A.: Chemistry of atmospheric brown carbon, *Chem. Rev.*,
729 115, 4335–4382, <https://doi.org/10.1021/cr5006167>, 2015.
- 730 Laskin, A., West, C. P., and Hettiyadura A. P. S.: Molecular insights into the composition, sources,
731 and aging of atmospheric brown carbon, *Chem. Soc. Rev.*, 54, 1583,
732 <https://doi.org/10.1039/d3cs00609c>, 2025.
- 733 Liu, J., Bergin, M., Guo, H., King, L., Kotra, N., Edgerton, E., and Weber, R. J.: Size-resolved
734 measurements of brown carbon in water and methanol extracts and estimates of their
735 contribution to ambient fine-particle light absorption, *Atmos. Chem. Phys.*, 13, 12389–12404,
736 <https://doi.org/10.5194/acp-13-12389-2013>, 2013.
- 737 Liu, J., Lin, P., Laskin, A., Laskin, J., Kathmann, S. M., Wise, M., Caylor, R., Imholt, F., Selimovic,
738 V., and Shilling, J. E.: Optical properties and aging of light-absorbing secondary organic
739 aerosol, *Atmos. Chem. Phys.*, 16, 12815–12827, <https://doi.org/10.5194/acp-16-12815-2016>,
740 2016.
- 741 Liu, S., Aiken, A. C., Gorkowski, K., Dubey, M. K., Cappa, C. D., Williams, L. R., Herndon, S. C.,
742 Massoli, P., Fortner, E. C., Chhabra, P. S., Brooks, W. A., Onasch, T. B., Jayne, J. T., Worsnop,
743 D. R., China, S., Sharma, N., Mazzoleni, C., Xu, L., Ng, N. L., Liu, D., Allan, J. D., Lee, J. D.,
744 Fleming, Z. L., Mohr, C., Zotter, P., Szidat, S., and Prévôt, A. S. H.: Enhanced light absorption
745 by mixed source black and brown carbon particles in UK winter, *Nat. Commun.*, 6, 8435,
746 <https://doi.org/10.1038/ncomms9435>, 2014.
- 747 Mo, Y., Li, J., Zhong, G., Zhu, S., Zhao, S., Tang, J., Jiang, H., Cheng, Z., Tian, C., Chen, Y., and
748 Zhang, G.: The water-insoluble organic carbon in PM_{2.5} of typical Chinese urban areas: light-
749 absorbing properties, potential sources, radiative forcing effects, and a possible light-absorbing
750 continuum, *Atmos. Chem. Phys.*, 24, 7755–7772, <https://doi.org/10.5194/acp-24-7755-2024>,
751 2024.
- 752 National Public Service Platform for Standards Information, Ambient Air Quality Standards,
753 <https://std.samr.gov.cn/gb/search/gbDetailed?id=4348B721E78BA160E06397BE0A0A32BA>,
754 2025.



- 755 Petzold, A., Ogren, J. A., Fiebig, M., Laj, P., Li, S. M., Baltensperger, U., Holzer-Popp, T., Kinne,
756 S., Pappalardo, G., Sugimoto, N., Wehrli, C., Wiedensohler, A., and Zhang, X. Y.:
757 Recommendations for reporting "black carbon" measurements, *Atmos. Chem. Phys.*, 13,
758 8365–8379, <https://doi.org/10.5194/acp-13-8365-2013>, 2013.
- 759 Pileci, R. E., Modini, R. L., Bertò, M., Yuan, J., Corbin, J. C., Marinoni, A., Henzing, B., Moerman,
760 M. M., Putaud, J. P., Spindler, G., Wehner, B., Müller, T., Tuch, T., Trentini, A., Zanatta, M.,
761 Baltensperger, U., and Gysel-Beer, M.: Comparison of co-located refractory black carbon (rBC)
762 and elemental carbon (EC) mass concentration measurements during field campaigns at several
763 European sites, *Atmos. Meas. Tech.*, 14, 1379–1403, [https://doi.org/10.5194/amt-14-1379-](https://doi.org/10.5194/amt-14-1379-2021)
764 2021, 2021.
- 765 Pöschl, U.: Atmospheric aerosols: composition, transformation, climate and health effects, *Angew.*
766 *Chem. Int. Ed.*, 44, 7520–7540, <https://doi.org/10.1002/anie.200501122>, 2005.
- 767 Putaud, J. P., Cavalli, F., Yttri, K. E., Chow, J. C., Watson, J. G., Sinha, B., Venkataraman, C.,
768 Ikemori, F., Jaffrezo, J. L., Uzu, G., Moreno, I., Krejci, R., Laj, P., Gupta, T., Hu, M., Kim, S.
769 W., Mayol-Bracero, O., Quinn, P., Aas, W., Alastuey, A., Andrade, M., Angelucci, M., Anurag,
770 G., Beukes, J. P., Bhardwaj, A., Chatterjee, A., Chaudhary, P., Chhangani, A. K., Conil, S.,
771 Degorska, A., Devaliya, S., Dhandapani, A., Duhan, S. S., Dumka, U. C., Habib, G., Hamzavi,
772 Z., Haswani, D., Herrmann, H., Holubova, A., Hueglin, C., Imran, M., Jehangir, A., Kapoor, T.
773 S., Karanasiou, A., Khaiwal, R., Kim, J., Kolesa, T., Kozakiewicz, J., Kranjc, I., Laura, J. S.,
774 Lian, Y., Liu, J. W., Manwani, P., Mardoñez-Balderrama, V., Marticorena, B., Matsuki, A., Mor,
775 S., Mukherjee, S., Murthy, S., Muthalagu, A., Najar, T. A., Kumar, R. N., Pandithurai, G., Perez,
776 N., Phairuang, W., Phuleria, H. C., Poulain, L., Prasad, L., Pullokaran, D., Qadri, A. M.,
777 Qureshi, A., Ramirez, O., Roy, S., Rüdiger, J., Saikia, B. K., Saikia, P., Sauvage, S., Savvides,
778 C., Sharma, R., Singh, T., Singh, G. K., Spoor, R., Srivastava, A. K., Raman, R. S., Van Zyl, P.
779 G., Vecchiocattivi, M., Voiron, C., Xin, J. Y., and Yadav, K.: A worldwide aerosol
780 phenomenology: elemental and organic carbon in PM_{2.5} and PM₁₀, *Atmos. Environ.*, 358,
781 121338, <https://doi.org/10.1016/j.atmosenv.2025.121338>, 2025.
- 782 Putaud, J. P., Van Dingenen, R., Alastuey, A., Bauer, H., Birmili, W., Cyrys, J., Flentje, H., Fuzzi, S.,
783 Gehrig, R., Hansson, H. C., Harrison, R. M., Herrmann, H., Hitzenberger, R., Hüglin, C., Jones,
784 A. M., Kasper-Giebl, A., Kiss, G., Koussa, A., Kuhlbusch, T. A. J., Löschau, G., Maenhaut, W.,



- 785 Molnar, A., Moreno, T., Pekkanen, J., Perrino, C., Pitz, M., Puxbaum, H., Querol, X.,
786 Rodriguez, S., Salma, I., Schwarz, J., Smolik, J., Schneider, J., Spindler, G., ten Brink, H.,
787 Tursic, J., Viana, M., Wiedensohler, A., and Raes, F.: A European aerosol phenomenology-3:
788 Physical and chemical characteristics of particulate matter from 60 rural, urban, and kerbside
789 sites across Europe, *Atmos. Environ.*, 44, 1308–1320, 2010.
- 790 Renzi, L., Di Biagio, C., Heuser, J., Zanatta, M., Cazaunau, M., Bergé, A., Pangui, E., Yon, J.,
791 Isolabella, T., Massabò, D., Vernocchi, V., Mazzini, M., Vogel, F., Yu, C., Formenti, P., Picquet-
792 Varrault, B., Doussin, J. F., and Marinoni, A.: The role of size in the multiple scattering
793 correction C for dual-spot aethalometer: a field and laboratory investigation, *Atmos. Meas.*
794 *Tech.*, 19, 1365–1383, <https://doi.org/10.5194/amt-19-1365-2026>, 2026.
- 795 Samset, B. H., Myhre, G., Herber, A., Kondo, Y., Li, S. M., Moteki, N., Koike, M., Oshima, N.,
796 Schwarz, J. P., Balkanski, Y., Bauer, S. E., Bellouin, N., Berntsen, T. K., Bian, H., Chin, M.,
797 Diehl, T., Easter, R. C., Ghan, S. J., Iversen, T., Kirkevåg, A., Lamarque, J. F., Lin, G., Liu, X.,
798 Penner, J. E., Schulz, M., Seland, Ø., Skeie, R. B., Stier, P., Takemura, T., Tsigaridis, K., and
799 Zhang, K.: Modelled black carbon radiative forcing and atmospheric lifetime in AeroCom
800 Phase II constrained by aircraft observations, *Atmos. Chem. Phys.*, 14, 12465–12477,
801 <https://doi.org/10.5194/acp-14-12465-2014>, 2014.
- 802 Sedlacek III, A. J., Buseck, P. R., Adachi, K., Onasch, T. B., Springston, S. R., and Kleinman, L.:
803 Formation and evolution of tar balls from northwestern US wildfires, *Atmos. Chem. Phys.*, 18,
804 11289–11301, <https://doi.org/10.5194/acp-18-11289-2018>, 2018.
- 805 Snyder, D. C., and Schauer, J. J.: An inter-comparison of two black carbon aerosol instruments and
806 a semi-continuous elemental carbon instrument in the urban environment, *Aerosol Sci.*
807 *Technol.*, 41, 463–474, <https://doi.org/10.1080/02786820701222819>, 2007.
- 808 Tinorua, S., Denjean, C., Nabat, P., Pont, V., Arnaud, M., Bourrienne, T., Dias Alves, M., and
809 Gardrat, E.: A 2-year intercomparison of three methods for measuring black carbon
810 concentration at a high-altitude research station in Europe, *Atmos. Meas. Tech.*, 17, 3897–3915,
811 <https://doi.org/10.5194/amt-17-3897-2024>, 2024.
- 812 Tuccella, P., Di Antonio, L., Di Muzio, A., Colaiuda, V., Lidori, R., Menut, L., Pitari, G., and
813 Raparelli, E.: Modeling the black and brown carbon absorption and their radiative impact: the



- 814 June 2023 intense Canadian boreal wildfires case study, *J. Geophys. Res. Atmos.*, 130,
815 e2024JD042674, <https://doi.org/10.1029/2024JD042674>, 2025.
- 816 van der Velde, I. R., van der Werf, G. R., Houweling, S., Eskes, H. J., Veeffkind, J. P., Borsdorff, T.,
817 and Aben, I.: Biomass burning combustion efficiency observed from space using
818 measurements of CO and NO₂ by the TROPOspheric Monitoring Instrument (TROPOMI),
819 *Atmos. Chem. Phys.*, 21, 597–616, <https://doi.org/10.5194/acp-21-597-2021>, 2021.
- 820 Wang, Y. Y., Zheng, Z. H., Sun, Y., Yao, Y., Ma, P. L., Zhang, A. X., ; Zhu, S. P., Zhang, Z. X., Chen,
821 X. Y., Pang, Y. E., Wang, Q. Y., Che, H. Z., Ching, J., and Li, W. J.: Improved representation
822 of black carbon mixing structures suggests stronger direct radiative heating, *One Earth*, 8,
823 101311, <https://doi.org/10.1016/j.oneear.2025.101311>, 2025.
- 824 Washenfelder, R. A., Attwood, A. R., Brock, C. A., Guo, H., Xu, L., Weber, R. J., Ng, N. L., Allen,
825 H. M., Ayres, B. R., Baumann, K., Cohen, R. C., Draper, D. C., Duffey, K. C., Edgerton, E.,
826 Fry, J. L., Hu, W. W., Jimenez, J. L., Palm, B. B., Romer, P., Stone, E. A., Wooldridge, P. J.,
827 and Brown, S. S.: Biomass burning dominates brown carbon absorption in the rural
828 southeastern United States, *Geophys. Res. Lett.*, 42, 653–664,
829 <https://doi.org/10.1002/2014GL062444>, 2015.
- 830 Weingartner, E., Saathoff, H., Schnaiter, M., Streit, N., Bitnar, B., and Baltensperger, U.: Absorption
831 of light by soot particles: determination of the absorption coefficient by means of aethalometers,
832 *J. Aerosol Sci.*, 34, 1445–1463, [https://doi.org/10.1016/S0021-8502\(03\)00359-8](https://doi.org/10.1016/S0021-8502(03)00359-8), 2003.
- 833 Winiger, P., Barrett, T. E., Sheesley, R. J., Huang, L., Sharma, S., Barrie, L. A., Yttri, K. E.,
834 Evangeliou, N., Eckhardt, S., Stohl, A., Klimont, Z., Heyes, C., Semiletov, I. P., Dudarev, O.
835 V., Charkin, A., Shakhova, N., Holmstrand, H., Andersson, A., and Gustafsson, Ö.: Source
836 apportionment of circum-Arctic atmospheric black carbon from isotopes and modeling, *Sci.*
837 *Adv.*, 5, eaau8052, <https://doi.org/10.1126/sciadv.aau8052>, 2019.
- 838 Wu, X., Cao, F., Haque, M., Fan, M. Y., Zhang, S. C., and Zhang, Y. L.: Molecular composition and
839 source apportionment of fine organic aerosols in Northeast China, *Atmos. Environ.*, 239,
840 117722, <https://doi.org/10.1016/j.atmosenv.2020.117722>, 2020.
- 841 Xiao, Q. Y., Geng, G. N., Xue, T., Liu, S. G., Cai, C. L., He, K. B., and Zhang, Q.: Tracking PM_{2.5}
842 and O₃ pollution and the related health burden in China 2013–2020, *Environ. Sci. Technol.*,
843 56, 6922–6932, <https://doi.org/10.1021/acs.est.1c04548>, 2022.



- 844 Xie, X. C., Zhang, Y. Z., Liang, R. S., Chen, W., Zhang, P. X., Wang, X., Zhou, Y., Cheng, Y., and
845 Liu, J. M.: Wintertime heavy haze episodes in Northeast China driven by agricultural fire
846 emissions, *Environ. Sci. Tech. Lett.*, 11, 150–157, <https://doi.org/10.1021/acs.estlett.3c00940>,
847 2024.
- 848 Yus-Díez, J., Bernardoni, V., Močnik, G., Alastuey, A., Ciniglia, D., Ivančič, M., Querol, X., Perez,
849 N., Reche, C., Rigler, M., Vecchi, R., Valentini, S., and Pandolfi, M.: Determination of the
850 multiple-scattering correction factor and its cross-sensitivity to scattering and wavelength
851 dependence for different AE33 Aethalometer filter tapes: a multi-instrumental approach,
852 *Atmos. Meas. Tech.*, 14, 6335–6355, <https://doi.org/10.5194/amt-14-6335-2021>, 2021.
- 853 Yus-Díez, J., Drinovec, L., Alados-Arboledas, L., Titos, G., Bazo, E., Casans, A., Patrón, D., Querol,
854 X., Gonzalez-Romero, A., Perez García-Pando, C., and Močnik, G.: Characterization of filter
855 photometer artifacts in soot and dust measurements – laboratory and ambient experiments
856 using a traceably calibrated aerosol absorption reference, *Atmos. Meas. Tech.*, 18, 3073–3093,
857 <https://doi.org/10.5194/amt-18-3073-2025>, 2025.
- 858 Zhang, J., Liu, L., Xu, L., Lin, Q., Zhao, H., Wang, Z., Guo, S., Hu, M., Liu, D., Shi, Z., Huang, D.,
859 and Li, W.: Exploring wintertime regional haze in northeast China: role of coal and biomass
860 burning, *Atmos. Chem. Phys.*, 20, 5355–5372, <https://doi.org/10.5194/acp-20-5355-2020>,
861 2020.
- 862 Zhang, X. L., Lin, Y. H., Surratt, J. D., Zotter, P., Prévôt, A. S. H., and Weber, R. J.: Light-absorbing
863 soluble organic aerosol in Los Angeles and Atlanta: a contrast in secondary organic aerosol,
864 *Geophys. Res. Lett.*, 38, L21810, <https://doi.org/10.1029/2011GL049385>, 2011.
- 865 Zhong, Q. R., Schutgens, N., van der Werf, G. R., Takemura, T., van Noije, T., Mielonen, T., Checa-
866 Garcia, R., Lohmann, U., Kirkevåg, A., Olivie, D. J. L., Kokkola, H., Matsui, H., Kipling, Z.,
867 Ginoux, P., Le Sager, P., Rémy, S., Bian, H. S., Chin, M., Zhang, K., Bauer, S. E., and Tsigaridis,
868 K.: Threefold reduction of modeled uncertainty in direct radiative effects over biomass burning
869 regions by constraining absorbing aerosols, *Sci. Adv.*, 9, eadi3568,
870 <https://doi.org/10.1126/sciadv.adi3568>, 2023.